Self-organized epigenetic signal processing in active chromatin

Xu-Ze Zhang,[1] Hai-Zhen Long,[2] Hao-Yue Zhang,[2] and Kai Huang[1,*]

[1] *Institute of Systems and Physical Biology, Shenzhen Bay Laboratory, Shenzhen 518132, China.*
[2] *Institute of Molecular Physiology, Shenzhen Bay Laboratory, Shenzhen 518132, China.*

(Dated: September 3, 2026)

Active histone marks turn over rapidly in open chromatin, yet their states do not simply track the instantaneous regulatory input and can retain information about prior stimulation. We develop a theoretical framework that separates this external input $a(\tau)$ from a state-dependent spatial amplification $\mathcal{G}(m)$, through which existing marks reshape local factor availability. A sufficiently steep increase in $\mathcal{G}(m)$ generates two thresholds that partition inputs into OFF, MEMORY, and ON regimes, governing mark erasure, history-dependent maintenance, and establishment. In a microscopic polymer model with epigenetic switching, marked chromatin and mobile factors self-organize into a localized reaction hub, thereby generating the required nonlinear $\mathcal{G}(m)$. Measured directly from microscopic configurations, this constitutive relation enables quantitative predictions of deterministic regime boundaries, first-passage statistics, recovery after perturbation, and frequency-dependent hysteresis without additional fitting. The resulting response architecture allows strong inputs to establish a high-mark state, weaker inputs to maintain it while limiting off-target spreading, and repeated inputs to be integrated over time. These results identify self-organized spatial feedback as a minimal mechanism for epigenetic signal processing in active chromatin.

I. INTRODUCTION

Chromatin regions can occupy distinct epigenetic states, characterized in part by specific patterns of histone modifications [1, 2]. These states participate in the regulation of gene expression during development, cell-state transitions, and responses to environmental signals [3]. Unlike the static DNA sequence, histone modifications are dynamically changed on cellular timescales [4]. A central physical question is therefore how biochemical reactions and three-dimensional chromatin organization couple regulatory signals to the establishment, maintenance, and erasure of epigenetic states despite continuous turnover [5–9].

For repressive histone marks such as H3K9me3 and H3K27me3 [10], substantial progress has established a key physical picture. Central to this picture is reader–writer feedback, in which a modified nucleosome promotes the deposition of identical marks on nearby chromatin [11–14]. Coupled with 3D chromatin folding [15], this feedback extends beyond genomic neighbors to act through spatial contacts between distant loci. Theoretical models show that this reciprocal coupling can drive the *de novo* establishment and self-organization of coherent epigenetic domains [16]. A major question in these systems is how such domains persist through molecular turnover and are restored after replication, thereby providing heritable *epigenetic memory* [7, 8, 17–20].

Whether the same coupling between mark dynamics and 3D chromatin folding operates in active chromatin remains unclear. In repressive systems such as heterochromatin, reader–writer feedback is often reinforced by self-compaction, creating a 3D structure that favors its own maintenance. By contrast, active chromatin is open and transcriptionally engaged [21]; its modifications, such as H3K27ac, turn over rapidly [22, 23], and locus-resolved measurements show unstable local retention of parental nucleosomes during replication [24]. An analogous feedback in active chromatin therefore cannot rely on a pre-existing compact domain or stable retention of parental nucleosomes. Instead, active marks are often treated primarily as downstream products or facilitators of transcription factor (TF) networks [25–27].

However, active-mark levels do not simply track instantaneous transcriptional activity, but evolve on distinct response and relaxation timescales. For example, neuronal depolarization induces near-peak H3K27ac levels at the *Fos* promoter and enhancers within 5 min before detectable mRNA accumulation [28]. Conversely, acute transcriptional inhibition does not markedly reduce global histone acetylation and can even enrich acetylation at active promoters, while CBP/p300 activity persists without ongoing transcription [29–31]. On longer timescales, active marks persist through mitosis to support bookmarking [32]. In transcriptional-memory systems, marks established by prior stimulation can remain after stimulus withdrawal and across multiple cell divisions, thereby priming faster and stronger responses to subsequent stimulation [33–35]. Thus, active chromatin is neither a passive transcriptional readout nor an autonomous memory element, but a regulated dynamical state that can retain information about prior stimulation. Active-mark dynamics therefore pose an input–output problem in which the response depends on both the current regulatory input and the existing mark state.

Several molecular mechanisms could allow the existing mark state to modify this input–output relation. First, active histone modifications engage in reader–writer interactions: CBP/p300 recognizes acetylated histone tails via its bromodomain to propagate acetylation [36, 37].

* huangkai@szbl.ac.cn

Second, acetylated chromatin recruits multivalent factors (e.g., BRD4, MED1 and p300) that assemble into dynamic, factor-rich structures [38–43]. Together, these findings point to a spatial feedback loop: active marks recruit writing factors, local factor enrichment accelerates further writing, and the modified chromatin stabilizes its own reaction environment. These processes, however, are embedded within locus-specific TF networks [44], so regulatory input, writing reactions, and chromatin–factor organization vary together. It is therefore difficult to determine whether factor-rich structures simply follow the regulatory input or generate an internal, state-dependent amplification that reshapes the writing response. Resolving this ambiguity requires a mesoscopic framework that separates the external regulatory input from the spatial amplification generated by the existing mark state.

Here, we present a minimal framework for self-organized epigenetic signal processing in active chromatin that explicitly separates an external regulatory input, $a(\tau)$, from a state-dependent spatial amplification, $\mathcal{G}(m)$, through which existing marks alter local factor availability. A sufficiently steep increase in $\mathcal{G}(m)$ generates two regulatory thresholds, partitioning inputs into OFF, MEMORY, and ON regimes that govern mark erasure, maintenance, and establishment. To test whether active chromatin can realize this response architecture, we construct a microscopic polymer model with mark-dependent factor recruitment and writing-loss reaction. The emergent chromatin–factor self-organization generates the required nonlinear $\mathcal{G}(m)$. When inserted into the theory, the measured $\mathcal{G}(m)$ quantitatively predicts deterministic regime boundaries and stochastic dynamics without additional fitting. The framework further accounts for recovery from mark loss, spatially selective maintenance and frequency dependence under repeated stimulation.

II. THEORETICAL FRAMEWORK AND MODELS

A. A mean-field theory of epigenetic-state dynamics

We begin with a general two-state description of local epigenetic-state dynamics. Each chromatin locus i carries a binary internal state x_i, with $x_i = 0$ denoting the unmarked state U_i and $x_i = 1$ the marked state M_i. The two states interconvert according to

$$U_i \underset{k_i^-(t)}{\overset{k_i^+(t)}{\rightleftharpoons}} M_i, \tag{1}$$

where the transition rates may depend on both the intrinsic reactivity of the locus and its instantaneous three-dimensional molecular environment. In the dilute, unsaturated limit, the writing rate can be expressed in terms of the local abundance of writing enzymes,

$$k_i^+(t) = w_i(t) q_W(\mathbf{R}_i, t), \tag{2}$$

where $w_i(t)$ denotes the local writing propensity and $q_W(\mathbf{R}_i, t)$ is the effective abundance of writing enzymes at locus i. Mark loss is coarse-grained as a spatially uniform first-order process, $k_i^-(t) = k_-$. This effective turnover accounts collectively for enzymatic erasure, histone replacement, and other processes that remove the mark [23, 45].

Consider a chromatin segment Ω containing N_Ω beads. Its instantaneous mark fraction is

$$\hat{m}(t) = \frac{1}{N_\Omega} \sum_{i=1}^{N_\Omega} x_i(t). \tag{3}$$

We denote its ensemble average by

$$m(t) = \langle \hat{m}(t) \rangle. \tag{4}$$

Its exact evolution follows directly from the bead-level transition dynamics:

$$\frac{dm}{dt} = \frac{1}{N_\Omega} \sum_{i=1}^{N_\Omega} \left\langle (1 - x_i) k_i^+(t) - x_i k_- \right\rangle. \tag{5}$$

We separate the local enzyme abundance into an overall density and a spatial enrichment factor:

$$q_W(\mathbf{R}, t) = \rho_W(t) V_\mathrm{K} \phi_W(\mathbf{R}, t), \tag{6}$$

where $\rho_W = N_W/V$ is the mean enzyme density, with N_W the number of writing enzymes and V is the confinement volume accessible to the factors. Here, V_K is the effective volume sampled by the short-ranged writing reaction, and ϕ_W is the dimensionless local enrichment relative to a spatially uniform enzyme distribution. Thus, $\rho_W V_\mathrm{K}$ specifies the expected local abundance in the uniform reference state, whereas ϕ_W captures its spatial redistribution.

The spatial distribution ϕ_W may depend on both the polymer conformation and the instantaneous enzyme positions. To derive a closed equation for the mark fraction, this microscopic spatial dependence must be reduced to a function of the instantaneous mark fraction. Because writing occurs only on unmarked beads, the relevant quantity is the mean enrichment sampled by those beads. For a prescribed value u of the instantaneous mark fraction, we define

$$\mathcal{G}(u) = \frac{1}{N_\Omega (1 - u)} \left\langle \sum_{i=1}^{N_\Omega} (1 - x_i) \phi_W(\mathbf{R}_i, t) \,\middle|\, \hat{m}(t) = u \right\rangle. \tag{7}$$

This conditional average characterizes the microscopic polymer and enzyme configurations at a given instantaneous mark fraction. We assume that the writing propensity is approximately uniform across the segment and

time-independent, $w_i(t) = w$. Under the constitutive assumptions that the conditional enrichment depends only on the instantaneous mark fraction and any residual dependence on other slow variables can be neglected, the ensemble-averaged dynamics can be written as

$$\frac{dm}{dt} = w\rho_W(t)V_{\mathrm{K}} \langle (1-\hat{m})\mathcal{G}(\hat{m})\rangle - k_- m. \tag{8}$$

We then apply the mean-field closure that neglects finite N_Ω fluctuations of the instantaneous mark fraction around its ensemble average,

$$\langle (1-\hat{m})\mathcal{G}(\hat{m})\rangle \simeq (1-m)\mathcal{G}(m), \tag{9}$$

which gives

$$\frac{dm}{dt} = w\rho_W(t)V_{\mathrm{K}}(1-m)\mathcal{G}(m) - k_- m. \tag{10}$$

We rescale time as $\tau = k_- t$ and define the dimensionless regulatory input

$$a(\tau) = \left.\frac{w\rho_W(t)V_{\mathrm{K}}}{k_-}\right|_{t=\tau/k_-}. \tag{11}$$

Eq. (10) then becomes

$$\frac{dm}{d\tau} = a(\tau)(1-m)\mathcal{G}(m) - m. \tag{12}$$

Eq. (12) is the deterministic mean-field limit of a state-dependent birth–death process, or equivalently a one-dimensional stochastic chemical reaction network [46, 47]. It separates the externally imposed regulatory input, $a(\tau)$, from the state-dependent spatial contribution, $\mathcal{G}(m)$. For constant a, a stationary mark fraction m^* is determined by the balance between writing and loss,

$$\frac{dm}{d\tau} = a(1-m^*)\mathcal{G}(m^*) - m^* = 0. \tag{13}$$

For a spatially uniform enzyme distribution, $\mathcal{G}(m) = 1$. Hence the system then has a unique stationary state, $m^* = a/(1+a)$. To characterize the nonlinear response generated by spatial recruitment, we define the input–state relation

$$g(m) \equiv \frac{m}{(1-m)\mathcal{G}(m)}. \tag{14}$$

Here, $g(m)$ is the regulatory input required to sustain a mark fraction m, and the stationary states at a given a satisfy $a = g(m^*)$.

A sufficiently strong positive feedback can make $g(m)$ nonmonotonic. Over a finite range of a, this produces three stationary states, with two stable states (m_L and m_H) separated by an unstable one (m_U), i.e., bistability. The resulting nonmonotonic response introduces two critical regulatory thresholds, a_{off} and a_{on}, with $a_{\mathrm{off}} < a_{\mathrm{on}}$. These thresholds partition the regulatory input into three functionally distinct regimes (Fig. 1A).

ON regime. When $a > a_{\mathrm{on}}$, only the high-mark state is stable. The regulatory input uniquely specifies an ON state and drives the system toward a high mark fraction, independently of its previous state.

OFF regime. When $a < a_{\mathrm{off}}$, only the low-mark state is stable. The regulatory input therefore uniquely specifies an OFF state, and the system is driven toward a low mark fraction regardless of its previous state.

MEMORY regime. When $a_{\mathrm{off}} < a < a_{\mathrm{on}}$, the low- and high-mark states are both stable. The instantaneous regulatory input alone no longer uniquely determines the state. Instead, the response also depends on the state already occupied by the system, which is subsequently maintained. This intermediate interval therefore constitutes a regulatory memory regime.

For repressive histone marks, reader–writer feedback coupled to three-dimensional chromatin compaction has already been shown to generate a sufficiently strong $\mathcal{G}(m)$ to support bistability [7, 8]. Because studies of these systems have largely focused on stable inheritance and epigenetic memory, attention has commonly centered on the intermediate MEMORY regime. Active histone marks provide a different starting point. Their regulatory inputs can change frequently and rapidly in response to environmental changes. Consequently, the significance of the nonlinear response lies not only in the existence of bistability, but also in how the system moves among the ON, OFF, and MEMORY regimes as the regulatory environment changes. This architecture allows regulatory signals of different strengths to establish, erase, or maintain an active chromatin state.

Whether active chromatin can generate spatial feedback sufficiently strong to realize this architecture remains unknown. In particular, it is unclear whether the required $\mathcal{G}(m)$ can emerge from the coupled dynamics of an open chromatin system and diffusing factors, rather than from a prescribed template. This motivates us to construct a more detailed microscopic model of the coupled chromatin–factor dynamics.

B. A microscopic model of active epigenetic-state dynamics

To determine $\mathcal{G}$, we construct a minimal active-chromatin polymer model in which factor recruitment, 3D polymer structure, and mark dynamics are explicitly coupled. The model is designed to implement the feedback

$$M \rightarrow \text{factor recruitment} \rightarrow \text{writing of nearby } U \rightarrow M \tag{15}$$

without an explicitly cooperative writing law. Its purpose is therefore to determine whether microscopic polymer–factor organization can generate a sufficiently strong $\mathcal{G}$ to produce the two regulatory thresholds a_{off} and a_{on}, thereby partitioning the input into ON, OFF, and MEMORY regimes.

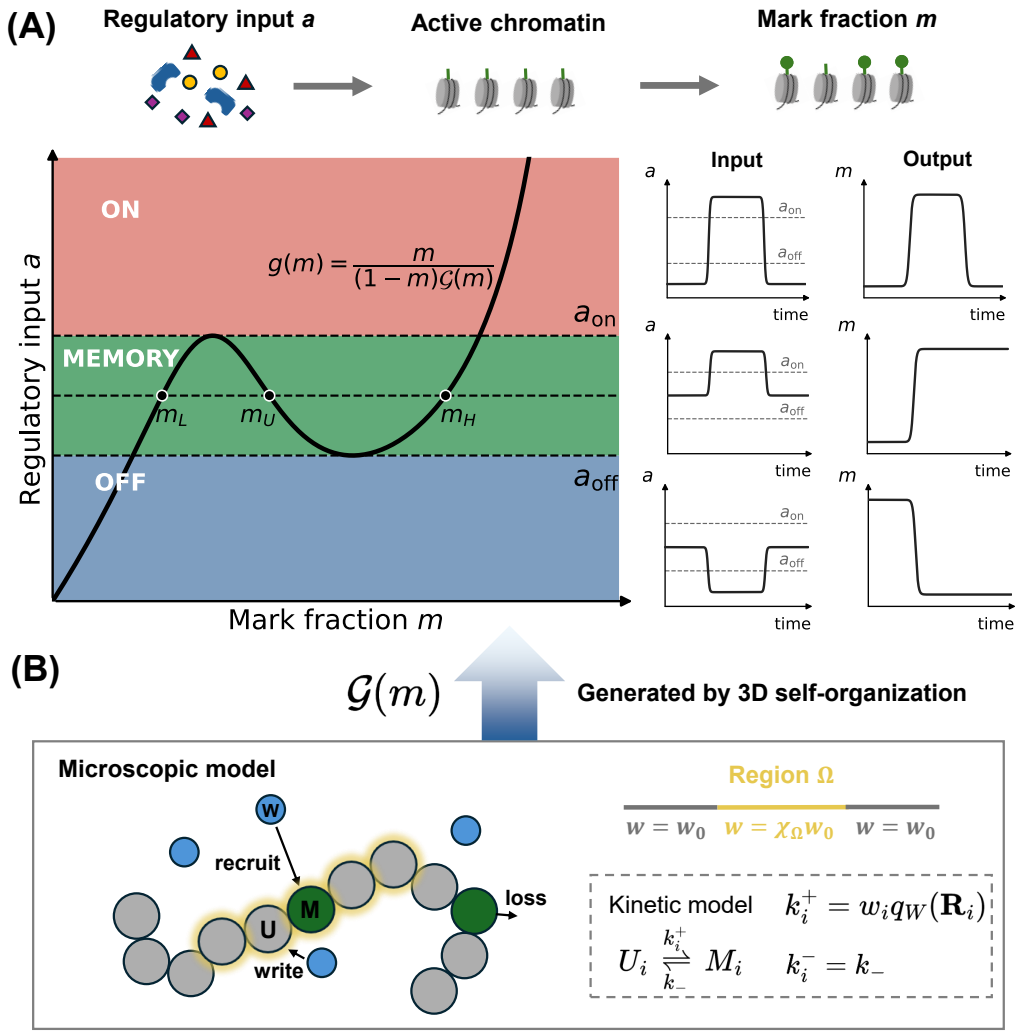

FIG. 1. **Active chromatin as a self-organized decoder of regulatory input.** (A) Top panel: A coarse-grained regulatory input a acts on active chromatin and is converted into the mark fraction m. Bottom left panel: The stationary condition $a = g(m) = m/[(1-m)\mathcal{G}(m)]$. A sufficiently strong state-dependent spatial contribution $\mathcal{G}(m)$ makes $g(m)$ nonmonotonic. Its local maximum and minimum define the thresholds $a_{\rm on}$ and $a_{\rm off}$, respectively, partitioning the regulatory input into three regimes. Above $a_{\rm on}$, only the high-mark state is stable (ON); below $a_{\rm off}$, only the low-mark state is stable (OFF); between the two thresholds, both states are stable (MEMORY). Bottom right panel: Schematic responses to time-dependent regulatory inputs. An input that moves from the OFF to the ON regime and then returns to the OFF regime establishes and subsequently erases the marked state (top). When the input crosses $a_{\rm on}$ and returns to the MEMORY regime, the established high-mark state is maintained (middle). Conversely, crossing $a_{\rm off}$ erases a pre-existing high-mark state, and the resulting low-mark state is maintained after the input returns to the MEMORY regime (bottom). (B) Microscopic realization of the spatial feedback. Chromatin beads interconvert between unmarked (U) and marked (M) states. Marked chromatin recruits mobile writing-related trans-factors W, whose local enrichment promotes writing of nearby unmarked chromatin at the rate $k_i^+ = w_i q_W(\mathbf{R}_i)$, while marks are continuously lost at the rate $k_i^- = k_-$. A focal region Ω receives an enhanced writing propensity, $w_i = \chi_\Omega w_0$, relative to the background $w_i = w_0$. The resulting three-dimensional chromatin–factor self-organization generates the state-dependent spatial contribution $\mathcal{G}(m)$ underlying the nonlinear response in (A).

We model a representative active-chromatin region as a flexible bead–spring polymer composed of N chromatin beads. Each bead carries a stochastic internal state, U or M, denoting the unmarked and marked states, respectively, with M representing a generic active histone modification. The polymer is surrounded by N_W mobile particles, denoted by W, which provide an effectively coarse-grained representation of writing-related trans-factors, including writing enzymes and other coactivators. In our model, we establish a hierarchy of nonbonded in-

teractions: trans-factors exhibit the strongest attraction toward marked chromatin ϵ_{MW}, followed by a weaker factor–factor self-association ϵ_{WW}, while all other background interactions remain weak (i.e., $\epsilon_{MW} > \epsilon_{WW} > \epsilon_{\text{other}}$).

The mark–factor attraction ϵ_{MW} is motivated by experimentally established interactions between active histone acetylation and transcriptional regulators. The p300/CBP bromodomain recognizes acetylated H3/H4 tails, while BRD4 binds preferentially to acetylation-enriched chromatin [36, 37, 42, 43]. Active-chromatin regulators, including BRD4, MED1, and p300, can also interact through multivalent protein–protein interactions and form factor-rich assemblies [38, 40, 41], motivating a finite factor–factor attraction ϵ_{WW}. In the present model, we choose $\epsilon_{MW} > \epsilon_{WW}$ to make mark-dependent recruitment the dominant source of feedback.

The chromatin states interconvert according to $U_i \underset{k_-}{\overset{k_i^+}{\rightleftharpoons}} M_i$, with a uniform mark-loss rate k_-. Consistent with the mean-field theory above, the writing rate is taken to be locally linear in the abundance of nearby W factors,

$$k_i^+ = w_i q_W(\mathbf{R}_i). \tag{16}$$

In the microscopic model, this abundance is evaluated from the instantaneous factor positions as

$$q_W(\mathbf{R}_i) = \sum_{j \in W} K(r_{ij}), \quad K(r) = \left(1 - \frac{r}{r_{\mathrm{K}}}\right) \Theta(r_{\mathrm{K}} - r), \tag{17}$$

where r_{ij} is the radial distance between chromatin bead i and factor j. Thus, the corresponding effective reaction volume is $V_{\mathrm{K}} \equiv \int_{\mathbb{R}^3} K(r)\, d\mathbf{r} = \frac{\pi r_{\mathrm{K}}^3}{3}$.

We focus on a prescribed chromatin segment Ω, within which the writing propensity is uniformly enhanced,

$$w_i = \begin{cases} \chi_\Omega w_0 & i \in \Omega, \\ w_0 & i \notin \Omega, \end{cases} \tag{18}$$

where w_0 is the background propensity and χ_Ω controls the relative reactivity of the focal segment. The segment Ω represents a locus selected by sequence-specific regulatory input, such as TF binding at an enhancer or promoter [48]. The global availability of trans-factors is controlled independently through their mean density, $\rho_W = N_W/V$. Thus, $\chi_\Omega w_0$, ρ_W, and k_- correspond directly to the quantities entering the regulatory input $a = \chi_\Omega w_0 \rho_W V_{\mathrm{K}}/k_-$.

The theoretical and microscopic descriptions are connected through the constitutive relation $\mathcal{G}$. From the simulated configurations, we measure the conditional enrichment of W factors sampled by unmarked beads in Ω at a given instantaneous mark fraction $\hat{m} = u$. The resulting $\mathcal{G}(u)$ is then inserted into Eq. (12) to predict the stationary points and saddle boundaries, which are subsequently tested against the full polymer simulations.

The polymer and trans-factors are evolved by Langevin molecular dynamics using HOOMD-blue [49], while the internal chromatin states are updated stochastically using the writing and loss rates evaluated from instantaneous configuration, $P = 1 - \exp(-\lambda \Delta t_{\text{update}})$, where $\lambda = k_i^+$ for a $U \to M$ transition and $\lambda = k_-$ for an $M \to U$ transition. Our reference system contains $N = 2000$ chromatin beads confined within a spherical volume, with a central segment of 50 beads designated as Ω. This geometry provides an effective representation of a localized active-chromatin region embedded within a larger polymer environment. Unless otherwise stated, the interaction parameters, system settings, and reaction rules are held fixed while χ_Ω and ρ_W are varied to control the regulatory input. Further simulation details are provided in Sec. I of the Supplemental Material (SM) [50].

III. RESULTS

A. Three-dimensional self-organization generates nonlinear response

We first examined the dynamical behavior of the microscopic model. Fig. 2A shows a kymograph of the mark states along the sequence for a representative parameter set, together with the instantaneous mark fraction $\hat{m}$ within Ω. The trajectory can be divided into three stages. Initially, stochastic writing and loss events produce sparse and short-lived marks. Following a sufficiently large fluctuation, the mark fraction increases rapidly and subsequently approaches a high-$\hat{m}$ plateau, while the marked beads remain largely confined to Ω.

Representative configurations reveal the spatial origin of this transition (Fig. 2A). As the local mark fraction increases, marked chromatin recruits additional trans-factors. Their local enrichment enhances writing on nearby unmarked chromatin, further increasing $\hat{m}$ and closing the positive-feedback loop. At high $\hat{m}$, marked chromatin and trans-factors co-organize into a localized three-dimensional reaction hub maintained under continuous writing and mark loss. The increase in mark fraction is accompanied by a decrease in the radius of gyration of region Ω (Fig. S4), showing that the chromatin conformation reorganizes together with factor recruitment. The writing activity within the hub is substantially higher than in the surrounding chromatin, allowing the marked state to persist despite ongoing turnover. Related factor-rich assemblies involving active chromatin and transcriptional coactivators have been extensively observed experimentally [38, 42].

Using the simulated configurations, we evaluated the conditional enrichment $\mathcal{G}(u)$ defined in Eq. (7) over a broad range of regulatory inputs a (Fig. 2B). At low u, $\mathcal{G}(u) \approx 1$, indicating weak factor enrichment around unmarked chromatin. It then increases sharply over an intermediate range of u and gradually saturates at high u.

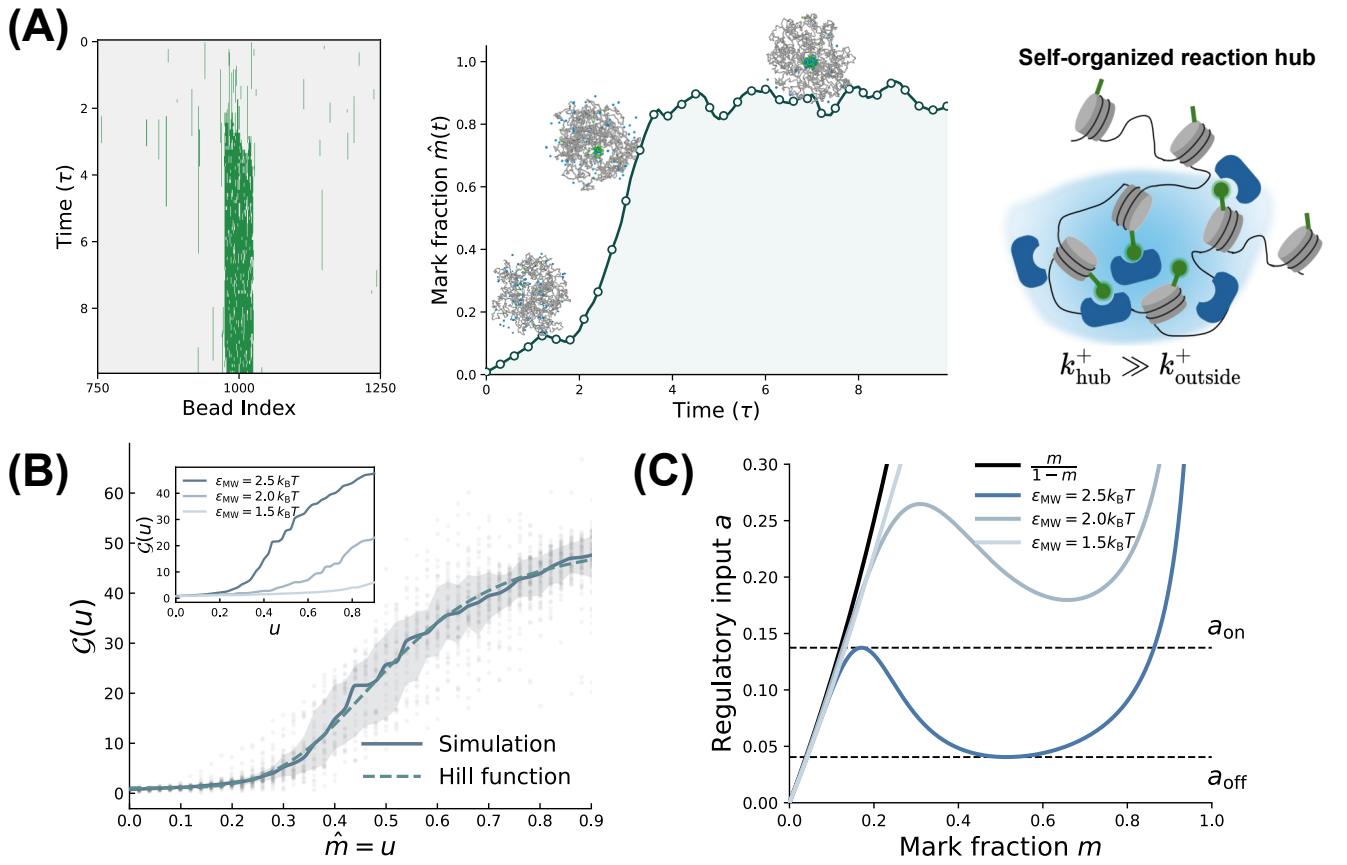

FIG. 2. **Three-dimensional self-organization generates a nonlinear regulatory response.** (A) Representative microscopic simulation trajectory. The kymograph shows the mark states along the chromatin sequence, and the corresponding mark fraction $\hat{m}$ within the focal region Ω is shown as a function of reduced time τ. Representative configurations illustrate the progressive recruitment of trans-factors and the formation of a localized high-mark state. Gray, green, and blue beads denote unmarked chromatin, marked chromatin, and trans-factors, respectively. The schematic illustrates the resulting self-organized reaction hub, within which the local writing rate is substantially higher than that in the surrounding chromatin, $k^+_{\mathrm{hub}} \gg k^+_{\mathrm{outside}}$. (B) Conditional factor enrichment $\mathcal{G}(u)$ measured from simulations across different (χ_Ω, ρ_W) conditions. Light-gray points show measurements from individual conditions, and the gray band denotes the 16th–84th percentile range across conditions. The blue solid curve is the parameter-balanced consensus. The dashed curve is a fit of Eq. (19) to this consensus, yielding $\mathcal{G}_{\min} = 1.08$, $A = 49.5$, $K = 0.511$, and $h = 4.34$. At a given u, the measured enrichment depends only weakly on (χ_Ω, ρ_W), supporting its representation by a common constitutive function $\mathcal{G}(u)$. Inset: reducing the mark–factor attraction ϵ_{MW} decreases both the amplitude and the steepness of $\mathcal{G}(u)$. (C) Stationary response functions $g(m) = m/[(1-m)\mathcal{G}(m)]$ obtained by evaluating the corresponding measured relations at $u = m$. The black curve shows the spatially uniform reference, $g_0(m) = m/(1-m)$, for $\mathcal{G}(m) = 1$. For strong mark–factor attraction, $g(m)$ becomes nonmonotonic, with its local maximum and minimum defining a_{on} and a_{off}, respectively. Weakening ϵ_{MW} shifts the response upward and progressively eliminates the nonmonotonic interval.

This response is well described by the Hill function

$$\mathcal{G}(u) = \mathcal{G}_{\min} + A\frac{u^h}{K^h + u^h}, \tag{19}$$

Although the enrichment could in principle depend on both the mark fraction and the regulatory input, $\mathcal{G} = \mathcal{G}(u, a)$, its measured value at a given u is nearly independent of a (Fig. S2). Data obtained under different regulatory inputs therefore fall approximately on a common $\mathcal{G}(u)$ curve. This supports treating the instantaneous mark fraction as a sufficient coarse-grained variable for closing the microscopic spatial dynamics.

The inset of Fig. 2B shows the effect of varying the mark–factor attraction ϵ_{MW}. Reducing ϵ_{MW} weakens the recruitment of trans-factors by marked chromatin, thereby decreasing both the amplitude and the steepness of $\mathcal{G}(u)$. This result identifies $\mathcal{G}(u)$ as a constitutive relation determined by the microscopic interactions and spatial organization of the system. By comparison, varying the factor–factor attraction ϵ_{WW} produces a weaker change in $\mathcal{G}(u)$ over the parameter range examined (Fig. S5A).

Finally, we evaluated the measured and fitted $\mathcal{G}(u)$ at $u = m$ and inserted the resulting $\mathcal{G}(m)$ into Eq. (13)

(Fig. 2C). For the spatially uniform reference with $\mathcal{G}(m) = 1$, the resulting function $g_0(m) = m/(1-m)$ increases monotonically and generates a single stationary state for each a. For sufficiently strong mark–factor attraction, the measured $\mathcal{G}(m)$ instead produces a non-monotonic $g(m) = m/[(1-m)\mathcal{G}(m)]$, with a local maximum and minimum defining $a_{\rm on}$ and $a_{\rm off}$, respectively. As $\epsilon_{\rm MW}$ is reduced, the curve shifts upward, the separation between the two extrema narrows, and the non-monotonic region eventually disappears. The microscopic chromatin–factor dynamics therefore generates the feedback required for the saddle-node structure of the mean-field theory. We next test whether the resulting predictions agree quantitatively with the full microscopic simulations.

B. Microscopic realization of the three regulatory regimes

The microscopic model contains two main control parameters: the mean trans-factor density, ρ_W, and the writing propensity within Ω, $w = \chi_\Omega w_0$. For a fixed $\mathcal{G}(m)$, these quantities enter the theory only through the regulatory input $a = \chi_\Omega w_0 \rho_W V_{\rm K}/k_-$. The two saddle-node thresholds therefore define the following boundaries in the (χ_Ω, ρ_W) parameter space:

$$\rho_W^{\rm on}(\chi_\Omega) = \frac{a_{\rm on} k_-}{\chi_\Omega w_0 V_{\rm K}}, \qquad \rho_W^{\rm off}(\chi_\Omega) = \frac{a_{\rm off} k_-}{\chi_\Omega w_0 V_{\rm K}}. \tag{20}$$

Between these boundaries, both the low- and high-mark states are stable, and the current state depends on its previous state. Above the $a_{\rm on}$ boundary, only the high-mark state remains stable, whereas below the $a_{\rm off}$ boundary, only the low-mark state is stable.

To test these predictions in the microscopic model, we performed simulations across the (χ_Ω, ρ_W) parameter space using two initial conditions, $\hat{m}(0) = 0$ and $\hat{m}(0) = 1$, corresponding to fully unmarked and fully marked states, respectively. For each simulation trajectory k, the first-passage times are defined as

$$\begin{aligned} T_{L\to H}^{(k)} &= \inf\left\{\tau > 0 : \hat{m}^{(k)}(\tau) \geq m_{\rm th}^{L\to H}\right\}, \\ T_{H\to L}^{(k)} &= \inf\left\{\tau > 0 : \hat{m}^{(k)}(\tau) \leq m_{\rm th}^{H\to L}\right\}. \end{aligned} \tag{21}$$

The corresponding finite-time first-passage probabilities are

$$P_{X\to Y}(T_{\rm obs}) = \frac{1}{N_{\rm traj}} \sum_{k=1}^{N_{\rm traj}} \Theta\left(T_{\rm obs} - T_{X\to Y}^{(k)}\right), \tag{22}$$

where $X \to Y$ denotes either $L \to H$ or $H \to L$. Here, $P_{L\to H}$ is measured from $N_{\rm traj}$ trajectories initialized at $m(0) = 0$ and quantifies passage from the low-mark side across the threshold, whereas $P_{H\to L}$ is measured from $N_{\rm traj}$ trajectories initialized at $m(0) = 1$ and quantifies loss of the initially high-mark state. We set $m_{\rm th}^{L\to H} = 0.5$ and $m_{\rm th}^{H\to L} = 0.2$. An observation window of $T_{\rm obs} = 20$ in the reduced time $\tau = k_- t$ was used for both directions.

The simulated $P_{L\to H}$ and $P_{H\to L}$ are shown in Figs. 3A and 3B, respectively. For $P_{L\to H}$, nearly all trajectories cross the threshold at large w and high ρ_W, whereas reducing either parameter decreases the passage probability. The opposite trend is observed for $P_{H\to L}$. We overlaid the deterministic predictions $\rho_W^{\rm on}(\chi_\Omega)$ and $\rho_W^{\rm off}(\chi_\Omega)$ on the corresponding heat maps. Both curves closely track the regions in which the respective passage probabilities approach unity, showing that the mean-field theory captures the deterministic structure of the two-parameter space. However, the theory and simulation results represent different quantities. The thresholds $a_{\rm on}$ and $a_{\rm off}$ are saddle-node points of the deterministic equation for $N_\Omega \to \infty$, whereas the simulated observables are first-passage probabilities measured in a finite system over a finite observation window using prescribed mark-fraction thresholds. Their boundaries are therefore not expected to coincide exactly. In particular, changing $T_{\rm obs}$ shifts the transition boundary in the simulated heat maps (Fig. S7). We will treat the finite-system extension explicitly in the following subsection.

Finally, we combined the two heat maps into an RGB dynamical regime map (Fig. 3C). Red denotes $P_{L\to H} = 1$ and $P_{H\to L} = 0$, for which both initial conditions lead to, or remain in the high-mark state within the observation window. This behavior corresponds to the predicted ON regime. Blue denotes $P_{L\to H} = 0$ and $P_{H\to L} = 1$, for which both initial conditions lead to the low-mark state, corresponding to the OFF regime. Green denotes $P_{L\to H} = P_{H\to L} = 0$, indicating that both initial states are retained, as predicted for the MEMORY regime. Mixed colors near the boundaries reflect the finite stochastic system. The resulting map provides a microscopic realization of the three-regime structure predicted by the mean-field theory.

C. Finite-system dynamics and kinetic landscapes

Eq. (12) specifies the deterministic drift and fixed points of the mark fraction, corresponding to the macroscopic limit of the dynamics. A real chromatin region, however, contains a finite number of nucleosomes, and its state is observed over a finite timescale. We therefore construct a finite-N_Ω stochastic extension of Eq. (12). Let $n = 0, 1, \ldots, N_\Omega$ denote the number of marked sites within Ω, and let

$$m_n = \frac{n}{N_\Omega} \tag{23}$$

denote the mark fraction associated with state n. Let $p_n(\tau)$ be the probability of observing state n at time τ. Its evolution obeys

$$\frac{dp_n}{d\tau} = \lambda_{n-1} p_{n-1} + \mu_{n+1} p_{n+1} - (\lambda_n + \mu_n) p_n, \tag{24}$$

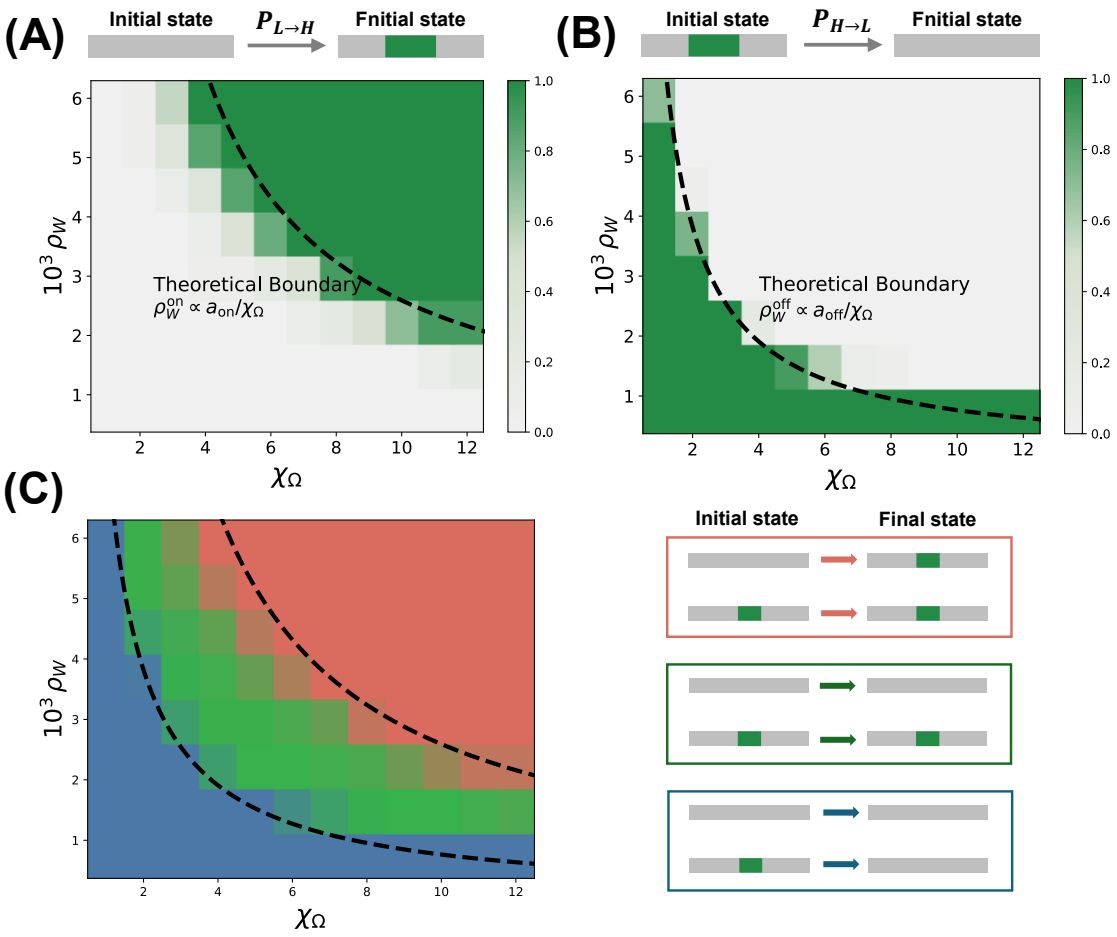

FIG. 3. **Microscopic realization of the ON, OFF, and MEMORY regimes.** (A) Finite-time passage probability $P_{L\to H}(T_{\rm obs})$ over the (χ_Ω, ρ_W) parameter space for simulations initialized in the fully unmarked state, $m(0) = 0$. Passage to the high-mark side is defined by the first crossing of $m_{\rm th}^{L\to H} = 0.5$. The black dashed curve denotes the mean-field ON boundary, $\rho_W^{\rm on}(\chi_\Omega) \propto a_{\rm on}/\chi_\Omega$. (B) Corresponding passage probability $P_{H\to L}(T_{\rm obs})$ for simulations initialized in the fully marked state, $m(0) = 1$, with passage to the low-mark side defined by $m_{\rm th}^{H\to L} = 0.2$. The black dashed curve denotes the mean-field OFF boundary, $\rho_W^{\rm off}(\chi_\Omega) \propto a_{\rm off}/\chi_\Omega$. An observation window of $T_{\rm obs} = 20$ in reduced time was used in both directions. (C) Dynamical regime map obtained by combining the two passage probabilities. Red denotes the ON regime, in which the high-mark state is established or retained; blue denotes the OFF regime, in which the low-mark state is established or retained; and green denotes the MEMORY regime, in which both initial states are retained. Mixed colors indicate stochastic transitions near the regime boundaries. The schematics illustrate the corresponding initial- and final-state relationships. Black dashed curves show the mean-field ON and OFF boundaries.

with the one-step birth and death rates

$$\lambda_n = (N_\Omega - n) a \mathcal{G}(m_n), \qquad \mu_n = n. \tag{25}$$

Eqs. (24) and (25) define a classical birth–death process for the mark number [46, 51, 52]. In the limit $N_\Omega \to \infty$, its macroscopic drift recovers Eq. (12). Related stochastic models have described nucleosome-modification dynamics by prescribing state-dependent transition rates, with cooperativity introduced directly into these rates to generate positive feedback and bistability [11, 52]. Here, the state dependence of the birth rate is instead supplied by $\mathcal{G}(m_n)$, which is measured independently from the microscopic chromatin–factor dynamics.

Solving Eq. (24) with an absorbing boundary at the prescribed threshold allows us to calculate rigorously the finite-time first-passage probability defined in Eq. (22). The left panels of Figs. 4A and 4B show the results for the $L \to H$ and $H \to L$ processes, respectively. When plotted against the regulatory input a, simulation results obtained from different combinations of (χ_Ω, ρ_W) approximately collapse onto a common curve. The finite-N_Ω theory quantitatively reproduces both directional probabilities without additional fitting. This collapse supports the identification of a as the effective variable controlling the mark dynamics and shows that the measured $\mathcal{G}$ is sufficient to predict the stochastic behavior of the finite

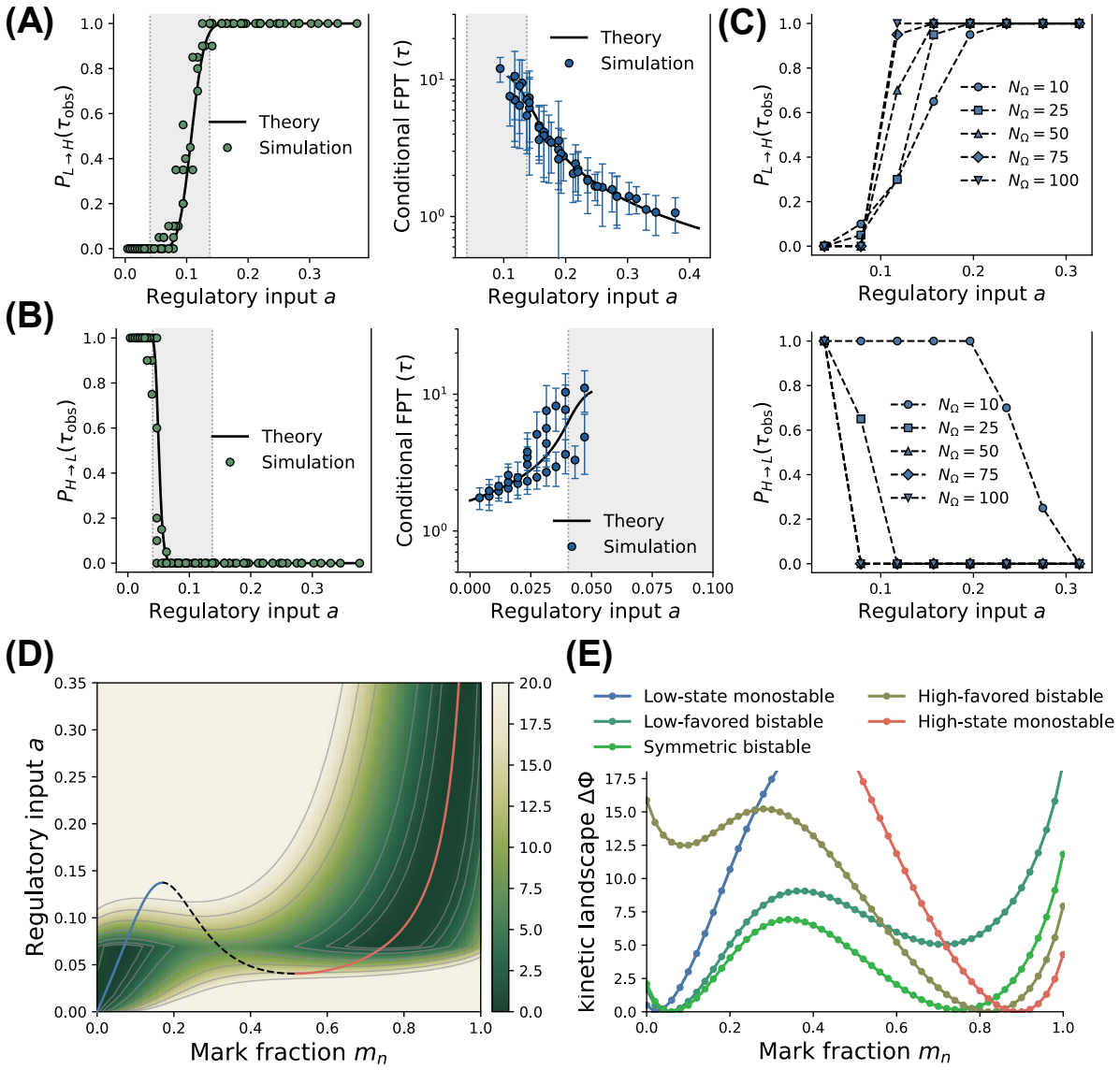

FIG. 4. **Finite-system transition dynamics and kinetic landscapes.** (A) Low-to-high passage statistics as functions of the regulatory input a. The left panel shows the finite-time first-passage probability $P_{L\to H}(T_{\rm obs})$, and the right panel shows the conditional mean first-passage time for trajectories that cross the prescribed threshold within the observation window. Symbols denote microscopic simulations obtained from different combinations of (χ_Ω, ρ_W), and solid curves are predictions of the finite-N_Ω master equation without additional fitting. (B) Corresponding high-to-low passage probability and conditional mean first-passage time. Conditional first-passage times in (A) and (B) are reported only when $P_{X\to Y}(T_{\rm obs}) > 0.5$; error bars show the standard deviations of the passage times. Gray shading marks the deterministic MEMORY regime, bounded by $a_{\rm off}$ and $a_{\rm on}$. (C) Simulated $P_{L\to H}(T_{\rm obs})$ (top) and $P_{H\to L}(T_{\rm obs})$ (bottom) for different region sizes N_Ω. The probability transitions become sharper as N_Ω increases, while their positions also vary because the constitutive relation $\mathcal{G}_{N_\Omega}(m)$ depends on region size. Dashed lines connect simulation points as guides to the eye. (D) Stationary kinetic landscape $\Delta\Phi(m_n; a)$ obtained from the finite-N_Ω master equation. Blue and red solid curves denote the low- and high-mark stable branches of the deterministic equation, respectively, and the black dashed curve denotes the unstable branch. Light-gray lines indicate contours of constant $\Delta\Phi$. (E) Landscape cross sections at five representative regulatory inputs, corresponding to low-state monostability, low-favored bistability, symmetric bistability, high-favored bistability, and high-state monostability.

system.

We further calculate the conditional mean first-passage time,

$$\langle T_{X\to Y}\rangle_{\rm cond} \equiv \mathbb{E}\left[T_{X\to Y} | T_{X\to Y} \le T_{\rm obs}\right]. \qquad (26)$$

Only trajectories that cross the threshold within the observation window contribute to the average. The theoretical and simulated conditional first-passage times are compared in the right panels of Figs. 4A and 4B, and

are reported only when $P_{X\to Y}(T_{\rm obs}) > 0.5$. The theory quantitatively reproduces the simulation results in both directions. Unlike the unconditional mean first-passage time $\langle T_{X\to Y}\rangle_\infty$, the conditional quantity in Eq. (26) is bounded by $T_{\rm obs}$ and therefore does not diverge as passage events become rare. The distinction between these two statistics is shown in Fig. S6.

The finite-system description also makes explicit how fluctuations in the mark fraction depend on region size. Over a short time interval $\Delta\tau$, Eq. (24) gives

$$\begin{aligned}\mathrm{Var}\left[\Delta\hat{m} \mid \hat{m}(\tau) = m_n\right] &= \frac{\lambda_n + \mu_n}{N_\Omega^2}\Delta\tau \\ &= \frac{a(1-m_n)\mathcal{G}_{N_\Omega}(m_n) + m_n}{N_\Omega}\Delta\tau + \mathcal{O}(\Delta\tau^2),\end{aligned} \tag{27}$$

where $\mathcal{G}_{N_\Omega}(m_n)$ emphasizes that the constitutive relation may itself depend on region size. For fixed transition rates, the amplitude of $\hat{m}$ fluctuations therefore decreases as $N_\Omega^{-1/2}$. Consistent with this dependence, the transitions of $P_{X\to Y}$ span progressively narrower ranges of a as N_Ω increases (Fig. 4C). The transition positions also vary with N_Ω because the measured $\mathcal{G}_{N_\Omega}(m_n)$ depends on region size (Fig. S5B); the size dependence of $P_{X\to Y}(T_{\rm obs})$ therefore reflects changes in both finite-number fluctuations and the spatial structures.

Having validated the finite-N_Ω description against the stochastic passage statistics, we use the same birth–death process to construct its stationary kinetic landscape. Let $\pi_n(a)$ denote the stationary probability of observing n marked sites at regulatory input a. For the discrete mark fraction m_n, we define

$$\Delta\Phi(m_n; a) = -\ln\left[\frac{\pi_n(a)}{\max\limits_{0\le k\le N_\Omega}\pi_k(a)}\right]. \tag{28}$$

Thus, $\Delta\Phi = 0$ at the most probable mark fraction for each a. This quantity is a kinetic quasipotential derived from the stationary distribution of the birth–death process, rather than a thermodynamic free energy.

Fig. 4D shows $\Delta\Phi(m_n; a)$ over the regulatory-input range, together with the stable and unstable fixed-point branches of the deterministic equation. The stable branches approximately trace the locations of the local basins, while the unstable branch lies near the intervening barrier. Within the MEMORY regime, the two basins are generally unequal in depth. Fig. 4E shows cross sections at five representative values of a, corresponding to low-state monostability, low-favored bistability, symmetric bistability, high-favored bistability, and high-state monostability. As a increases across the bistable interval, the relative depths of the two minima shift continuously from the low-mark basin to the high-mark basin (Fig. S8), producing corresponding changes in the escape barriers. The finite-system landscape therefore reveals differences in the relative stability of the two states and in the barriers for switching between them within the MEMORY regime.

D. Response to external perturbations

Active marks can be directly perturbed during transcription [53], replication [54], mitosis [32], and other processes. These perturbations affect mark levels in different ways: replication can substantially dilute local marks [24], whereas mitosis involves more complex changes. Here, we do not model these processes explicitly. Instead, we instantaneously delete a fraction $f_{\rm del}$ of the existing marks. The polymer and trans-factors are then allowed to relax with the mark reactions suspended, after which the reactions are resumed to determine whether the marked state recovers.

As illustrated in Fig. 5A, within the bistable regime the system is initially located at the high-state fixed point $m_{\rm H}$. Deleting a fraction $f_{\rm del}$ instantaneously reduces m to $(1-f_{\rm del})m_{\rm H}$. If the remaining mark fraction lies above the basin boundary $m_{\rm U}$, the system returns to the high-mark state; if it lies below $m_{\rm U}$, it evolves toward the low-mark state. The deterministic critical deletion fraction is therefore

$$f_{\rm del}^{\rm c}(a) = 1 - \frac{m_{\rm U}(a)}{m_{\rm H}(a)}. \tag{29}$$

We first tested this prediction in the symmetric bistable regime. After a moderate perturbation with $f_{\rm del} = 0.3$, the system remains within the high-mark basin and recovers its initial state (Fig. 5B). By contrast, a stronger perturbation with $f_{\rm del} = 0.7$ moves the system below the basin boundary, after which it relaxes to the low-mark state. The trajectory-averaged mark fraction in Fig. 5C shows the same behavior. At $f_{\rm del} = 0.5$, the perturbed state lies close to the basin boundary, and independent trajectories can evolve toward either state with comparable probabilities.

To quantify this stochastic response, we define $P_{\rm rec}(f_{\rm del}, a; T_{\rm obs})$ as the probability that a system initially in the high-mark state returns to that state after deletion. Fitting $P_{\rm rec}$ as a function of $f_{\rm del}$ gives an operational estimate of the critical deletion fraction, $f_{\rm del}^{50}$, defined by $P_{\rm rec}(f_{\rm del}^{50}, a; T_{\rm obs}) = 0.5$. A representative fit is shown in the inset of Fig. 5D.

Fig. 5D shows the resulting $f_{\rm del}^{50}$ over the bistable range of a. Consistent with the progression of kinetic landscapes in Fig. 4E, the deletion fraction tolerance increases with a: the high-mark state becomes progressively more resistant to mark loss as its basin expands. The deterministic prediction in Eq. (29) qualitatively captures this trend. We restrict $f_{\rm del}^{50}$ to the bistable regime, where it measures the boundary between two coexisting basins; in either monostable regime, no corresponding recovery threshold is defined.

E. Spatial specificity and dynamic regulation

The theory developed above coarse-grains three-dimensional chromatin organization into the dynamics of

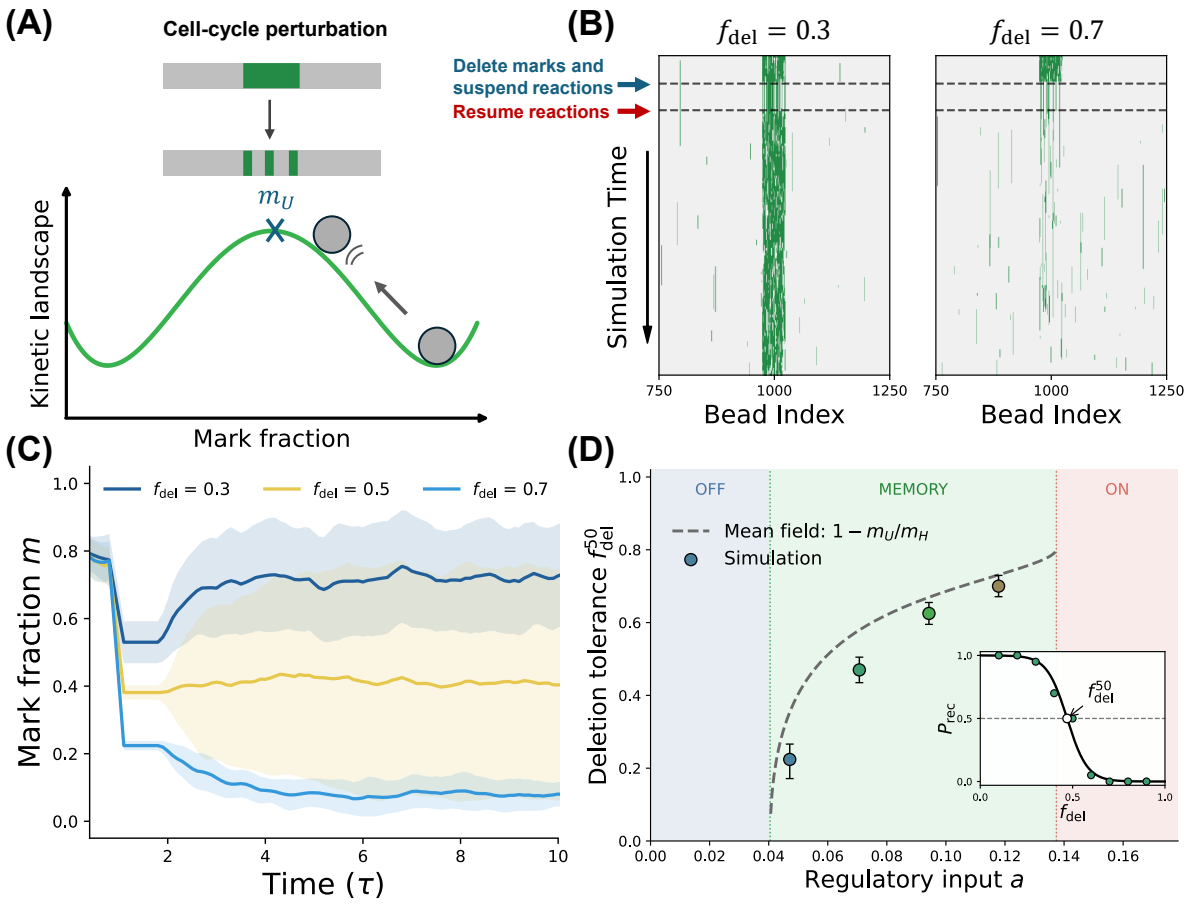

FIG. 5. **Response to external perturbations.** (A) Schematic representation of a cell-cycle-like mark-loss perturbation in the kinetic landscape. The system is initially located at the high-mark fixed point m_{H}. Deleting a fraction f_{del} of the existing marks reduces the mark fraction to $(1 - f_{\mathrm{del}})m_{\mathrm{H}}$. Recovery occurs if the perturbed state remains above the unstable fixed point m_{U} and therefore within the high-mark basin. (B) Representative kymographs following moderate and strong perturbations. Marks are deleted and mark reactions are suspended during the interval indicated by the dashed lines. After reactions are restored, the system either recovers the localized high-mark state for $f_{\mathrm{del}} = 0.3$ or relaxes to the low-mark state for $f_{\mathrm{del}} = 0.7$. (C) Trajectory-averaged mark fraction m following perturbations with different deletion fractions. Shaded regions indicate standard deviations across trajectories. (D) Deletion tolerance f_{del}^{50} as a function of the regulatory input a within the MEMORY regime. Symbols denote simulation results, and the gray dashed curve shows the deterministic prediction $f_{\mathrm{del}}^{\mathrm{c}} = 1 - m_{\mathrm{U}}/m_{\mathrm{H}}$. The inset illustrates the operational definition of f_{del}^{50} from the recovery probability, $P_{\mathrm{rec}}(f_{\mathrm{del}}^{50}) = 0.5$. Background colors indicate the deterministic OFF, MEMORY, and ON regimes. The recovery threshold is defined only in the bistable MEMORY regime.

the local mark fraction. It does not, however, resolve the distribution of marks outside the region Ω. Because spatially distant chromatin segments can contact Ω, writing can propagate to other positions along the polymer [7]. Parameter sets with comparable local mark fractions can therefore produce different spatial distributions of marks.

To quantify this distinction, we define the spatial specificity

$$S(t) = \sum_{i \in \Omega} x_i(t) / \sum_{i=1}^{N} x_i(t). \tag{30}$$

Here, $S = 1$ indicates that all marks are confined to Ω, whereas lower values indicate spreading into the surrounding chromatin. We report $S(T_{\mathrm{obs}})$ only for parameter sets that reliably establish a marked state within Ω. The resulting specificity over the (χ_Ω, ρ_W) parameter space is shown in Fig. 6A. At sufficiently high trans-factor densities, S decreases, indicating increased off-target deposition.

A representative spreading trajectory is shown in Fig. 6B. Marks are initially established within Ω. Chromatin segments outside Ω occasionally contact the marked region in three dimensions and acquire marks during these encounters. When the trans-factor pool is sufficiently large, these marks recruit additional factors and initiate the same feedback loop outside the region Ω. The propagation nevertheless remains limited rather

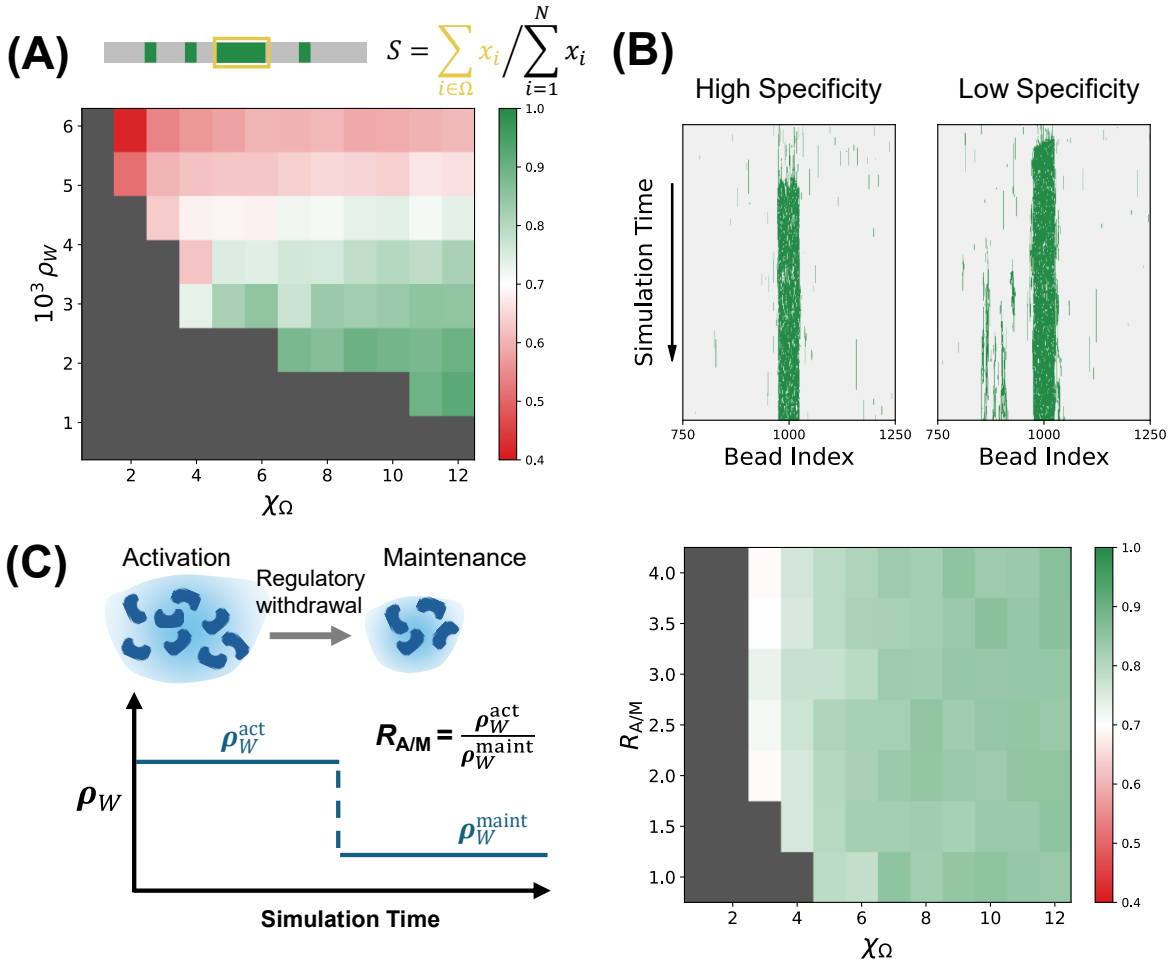

FIG. 6. **Spatial specificity and dynamic regulation.** (A) Spatial specificity $S(T_{\mathrm{obs}})$ over the (χ_Ω, ρ_W) parameter space, defined as the fraction of all marked sites that lie within the focal region Ω. Gray regions denote parameter sets for which a marked state is not established reliably and specificity is therefore not reported. Increasing the trans-factor density promotes off-target deposition and reduces spatial specificity. (B) Representative kymographs with high and low spatial specificity showing the propagation of marks from Ω to distal chromatin segments brought into spatial contact with the marked region. (C) Activation–maintenance switch for improving spatial specificity. A high trans-factor density ρ_W^{act} is applied during activation and subsequently reduced to ρ_W^{maint} during maintenance, with $R_{A/M} = \rho_W^{\mathrm{act}}/\rho_W^{\mathrm{maint}}$. The heat map shows the specificity measured at the end of the maintenance stage over the $(\chi_\Omega, R_{A/M})$ parameter space. Reducing the trans-factor density after activation suppresses off-target propagation while retaining the established marked state within Ω.

than extending over the entire polymer, because the finite trans-factor pool constrains the size of regions that can sustain this feedback simultaneously. This behavior is consistent with the role of limited enzyme availability in stabilizing repressive epigenetic domains [7]. Although χ_Ω and ρ_W enter the mean-field dynamics through the combined regulatory input $a \propto \chi_\Omega \rho_W$, they are not equivalent with respect to spatial specificity. Increasing ρ_W raises the availability of factors throughout the system. By contrast, increasing χ_Ω selectively enhances writing within Ω. It therefore strengthens the kinetic preference for the region Ω and preserves spatial specificity.

Increasing ρ_W promotes rapid and reliable establishment but also enhances spreading through three-dimensional contacts, producing a trade-off between establishment efficiency and spatial specificity. The separation between the establishment threshold a_{on} and the maintenance threshold a_{off} suggests a simple resolution. We consider a two-stage switch consisting of activation and maintenance. During activation, a high trans-factor density ρ_W^{act} drives the region Ω across the ON threshold. The density is subsequently reduced to ρ_W^{maint}, such that the established focal region remains in the MEMORY regime, whereas background regions enter the OFF regime. Off-target marks generated during activation can then no longer be maintained and are progressively removed by turnover.

We implemented this switch in the microscopic simulations and characterized the change in trans-factor density

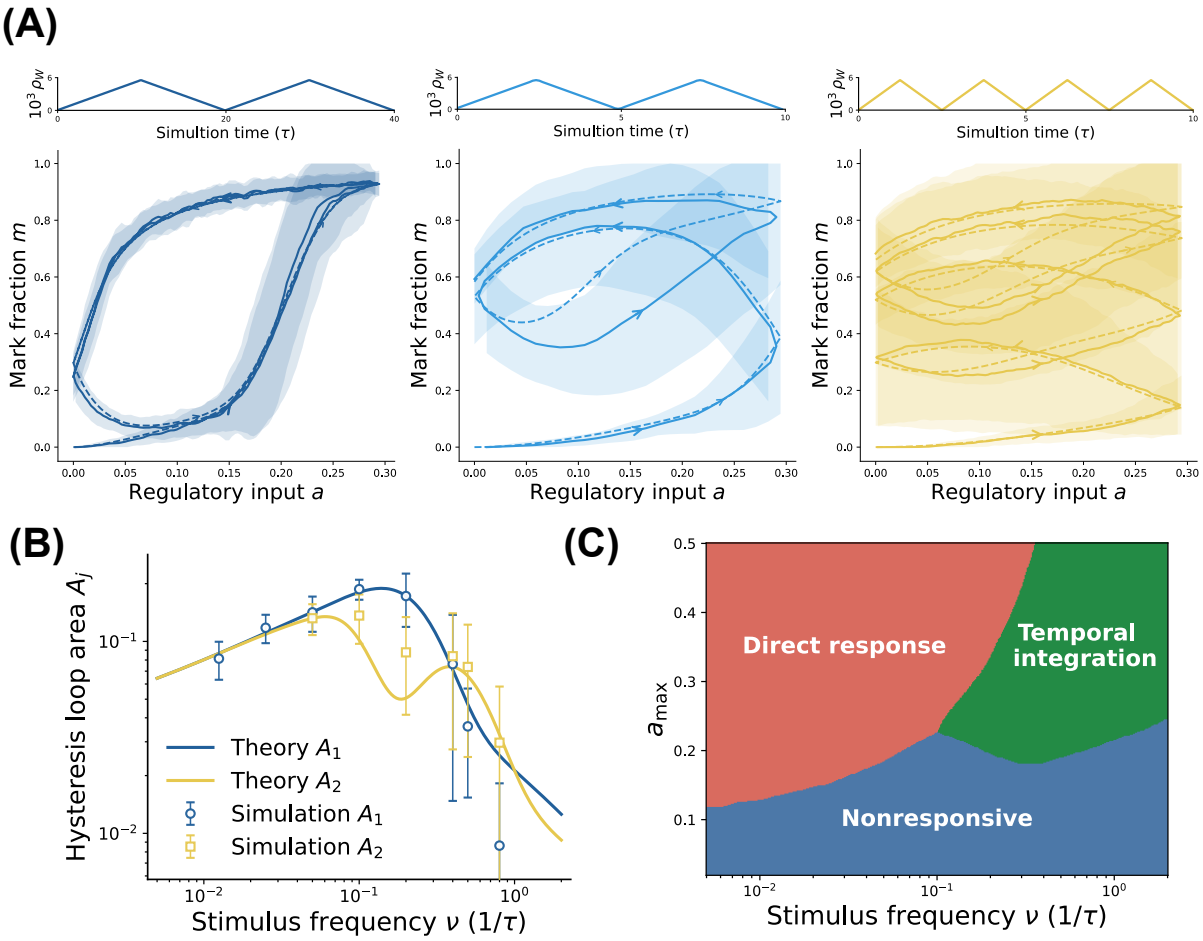

FIG. 7. **Frequency-dependent hysteresis and three regimes under dynamic stimulation.** (A) Mean mark-fraction responses to triangular-wave regulation at three representative frequencies. The upper panels show the imposed trans-factor density $\rho_W(\tau)$, and the lower panels show the resulting hysteresis loops obtained by plotting m against the instantaneous regulatory input a. Solid curves denote simulation averages, dashed curves are predictions of the finite-N_Ω master equation, and shaded regions indicate standard deviations across trajectories. Arrows indicate the direction of time. From left to right, the stimulus frequencies are $\nu = (1/20,\ 1/5,\ 1/2.5)\ \tau^{-1}$. (B) First- and second-cycle hysteresis areas, A_1 and A_2, as functions of stimulus frequency, with $A_j = |\oint_{C_j} \hat{m}\, da|$. Solid curves denote theoretical predictions, symbols denote simulation results, and error bars indicate standard deviations across independent trajectories. Both loop areas are reduced at excessively low and high frequencies, while the largest cycle-to-cycle difference occurs at an intermediate frequency. (C) Predicted dynamical response over the $(\nu, a_{\max})$ parameter space at fixed $a_{\min} = 0$, starting from the low-mark state. The activation cycle n_{act} is defined as the first cycle in which the predicted ensemble-averaged mark fraction exceeds the prescribed activation threshold m_{act}. Red denotes direct response, for which activation occurs during the first cycle; green denotes temporal integration, for which residual marks accumulate until activation occurs after multiple cycles; and blue denotes nonresponsive conditions, for which activation is not reached within the maximum observation window of 20 cycles.

by the activation-to-maintenance ratio

$$R_{A/M} = \frac{\rho_W^{\mathrm{act}}}{\rho_W^{\mathrm{maint}}}. \tag{31}$$

The spatial specificity was evaluated at the end of the maintenance stage. Fig. 6C shows S over the $(\chi_\Omega, R_{A/M})$ parameter space. A suitable activation-to-maintenance switch combines reliable establishment with spatially selective maintenance: the high activation density establishes the focal state, whereas the lower maintenance density suppresses off-target propagation while retaining the marked state within Ω.

F. Response under dynamic regulatory stimulation

Thus far, we have characterized the system under constant regulatory inputs or discrete switches between input levels. Regulatory activity in biological systems, however, can also vary continuously over relevant timescales [55–57]. We therefore examined the response

to a periodic regulatory stimulus. Specifically, $a(\tau)$ was varied linearly between fixed values $a_{\min}$ and $a_{\max}$ using a triangular waveform with stimulus frequency ν.

Fig. 7A shows the simulated m–a hysteresis loops at three representative frequencies. At low frequency, the system has sufficient time to establish and erase the marked state within each cycle. At an intermediate frequency, residual marks from the first cycle substantially alter the response during the subsequent cycle. At high frequency, a single cycle is too short for either establishment or erasure to be completed, and marks progressively accumulate over multiple cycles. We compared these results with the hysteresis loops obtained by solving Eq. (24) under the same time-dependent input. Using the independently measured $\mathcal{G}(u)$, the theory quantitatively reproduces the simulated loops without additional fitting.

To compare the dynamical responses across frequencies, we define the area enclosed by the jth hysteresis loop as

$$A_j = \left| \oint_{C_j} \hat{m}\, da \right|, \tag{32}$$

where C_j denotes the trajectory over cycle j. The loop area measures the path dependence of the response and reflects both the finite response time and the retention of the preceding state. Differences between successive loop areas provide a measure of how strongly one stimulation cycle modifies the response to the next.

Fig. 7B compares the theoretical and simulated values of A_1 and A_2, which again show quantitative agreement. Both excessively low and excessively high frequencies reduce the loop area. At low frequency, the mark fraction has sufficient time to follow the changing input, and the area decreases gradually. At high frequency, the mark fraction cannot respond appreciably within a single cycle, leading to a sharper reduction in area. At an intermediate frequency, A_1 reaches its maximum, and the difference $A_1 - A_2$ is also largest. The input period is then comparable to the intrinsic dynamical timescale of the mark fraction within Ω, producing the strongest cycle-to-cycle history dependence.

Hysteresis itself does not require a state-dependent $\mathcal{G}$. As shown in Fig. S9, models with constant $\mathcal{G} = 1$, 5, or 40 also produce frequency-dependent hysteresis. Varying the constant value can reproduce a similar range of loop areas, but no single constant $\mathcal{G}$ captures both their magnitude and the characteristic frequency observed in the simulations. The measured state-dependent $\mathcal{G}$ is therefore required to capture the characteristic frequency scale associated with the realistic cooperative response.

Finally, having validated the theory under time-dependent inputs, we used it to systematically examine the response over a broader range of stimulation amplitudes and frequencies. Starting from the low-mark state, we introduced an activation threshold $m_{\rm act}$ and defined $n_{\rm act}$ as the first stimulation cycle in which the predicted mark fraction exceeds this threshold. For each parameter set, the response was followed for a maximum of 20 cycles. Fig. 7C shows $n_{\rm act}$ over the $(a_{\max}, \nu)$ parameter space at fixed $a_{\min}$.

The response separates into three dynamical regimes. In the nonresponsive regime, the mark fraction does not cross the activation threshold within 20 cycles. In the direct-response regime, activation occurs during the first cycle. In the temporal-integration regime, a single cycle is insufficient for activation, but residual marks accumulate over repeated cycles until the threshold is crossed. If mark dynamics is viewed as a decoder of regulatory signals, the static ON, OFF, and MEMORY regimes specify the state structure under fixed inputs. Under time-dependent regulation, the response additionally depends on the competition between the input period and the intrinsic dynamical timescale of the marked region. The system can therefore extend its history dependence beyond the response to an instantaneous regulatory strength.

IV. DISCUSSION AND CONCLUSIONS

Previous physical theories of chromatin-based epigenetic memory have focused mainly on repressive marks and asked how a mark pattern can be preserved against turnover, replicative dilution, and other perturbations [7, 16–18]. These studies established that reader–writer feedback, three-dimensional spreading, chromatin compaction, and limited enzyme availability can stabilize marked domains over multiple cell generations. Recent particle-based models have made this spatial mechanism explicit. Polymer-assisted condensation of HP1 can create a liquid reaction container that restores diluted mark patterns, while Swi6-mediated condensation coupled to nucleosome reactions can generate bistable and spatially confined heterochromatic states [19, 20]. In their systems, the mark pattern is the information to be preserved, whereas external regulation is usually held fixed as a background condition or introduced only as a perturbation to the existing state. Active chromatin poses a different physical problem. Active-mark patterns commonly occupy smaller regulatory regions, such as enhancers and promoters, than the domains usually considered in repressive systems [7]. Active marks undergo rapid turnover within an open chromatin environment [22, 23, 28, 48]. At these scales, state fluctuations and local factor availability become important parts of the dynamics. Moreover, the mark state is continuously driven by locus-specific TFs and coactivators [44]. The relevant question is therefore not only whether an active mark state can persist, but how the existing chromatin state changes the response to subsequent regulatory input. Our framework makes this input explicit through $a(\tau)$ and separates it from the state-dependent spatial feedback $\mathcal{G}(m)$. This separation turns active-mark dynamics into an input–output problem: the external drive

supplies the regulatory signal, whereas the current mark state modifies its local reaction environment and thereby alters how that signal is decoded. Epigenetic memory then emerges as one regime of a broader response architecture that also governs state establishment, erasure, and even the processing of time-dependent inputs.

A possible physical basis for this state-dependent reaction environment is provided by the dynamic, factor-rich assemblies observed at active enhancers and promoters, where acetylated chromatin is enriched in BRD4, p300, MED1, and other transcriptional coactivators [38, 39, 42, 58–60]. Although these assemblies are often discussed as transcriptional condensates [38], how their three-dimensional organization contributes to epigenetic states remains incompletely understood. Our results suggest a possible epigenetic function for such assemblies: they can provide a local reaction environment in which the existing mark state controls the enrichment of writing factors and hence the rate of further mark deposition. Newly deposited marks then create additional recruitment sites, closing a positive spatial-feedback loop. This coupling is consistent with molecular mechanisms of histone acetylation regulation identified in recent experimental studies [36, 37, 60]. To quantify this feedback, we directly measured the conditional factor enrichment $\mathcal{G}(u)$ from the simulated configurations. In phenomenological models of epigenetic switching, nonlinear feedback is commonly prescribed through cooperative transition rates [11, 52]. Here, the local chromatin–factor interactions and reaction rules are specified, but the nonlinear dependence of $\mathcal{G}(m)$ on m is not. This relation emerges from the coupled chromatin–factor dynamics. Substituting the measured $\mathcal{G}(m)$ into the theory quantitatively predicts the deterministic regime and the finite-system switching probabilities and times, without additional fitting to these observables.

The magnitude and nonlinearity of $\mathcal{G}(u)$ are controlled by the molecular interactions that organize marked chromatin and trans-factors. In this model, the trans-factors W represent a heterogeneous mixture of writing enzymes and coactivators. Accordingly, ϵ_{WW} should be interpreted as the combined effect of molecular interactions. For histone acetylation, such interactions can arise from the intrinsically disordered regions of BRD4 and MED1, as well as from the disordered and structured interaction domains of p300 [38, 40, 61]. In our simulations, $\mathcal{G}(m)$ is more sensitive to ϵ_{MW} than to ϵ_{WW} over the parameter range examined. This does not imply a specific hierarchy between mark–factor and factor–factor interactions in biological systems. In cells, these interaction channels are likely to act together, with their relative contributions depending on molecular composition and regulatory context. Beyond molecular interactions, region size also affects the response through two distinct channels. It changes $\mathcal{G}_{N_\Omega}(m)$ by altering the capacity of the active region to organize a factor-rich structure, and it controls the amplitude of finite-number fluctuations, which decreases as $N_\Omega^{-1/2}$. This may provide insight into the size-dependent function of enhancers [62, 63].

The separation between the establishment threshold a_{on} and the maintenance threshold a_{off} assigns distinct biological functions to the ON, MEMORY, and OFF regimes. During development and differentiation, cell-fate commitment can require high levels of lineage-determining transcription factors [64, 65]. These dosage-dependent fate choices are consistent with the strong input required to cross a_{on}. Related establishment–maintenance asymmetries also occur in transcriptional memory systems [34]. In our model, however, the high trans-factor density that promotes reliable establishment also enhances off-target writing through three-dimensional contacts. The two thresholds enable a simple two-stage solution. A strong activation input first drives the focal region across a_{on}. The input is then lowered into the MEMORY regime, retaining the established focal state while placing background regions in the OFF regime. Off-target marks produced during establishment are consequently removed by turnover. Thus, temporal separation of establishment and maintenance improves the spatial specificity of the marked state.

Local active-mark levels can be perturbed by DNA replication, mitosis, and transcription-associated nucleosome turnover [23, 24, 32]. Although active domains lack the stable local recycling of parental nucleosomes observed in repressed chromatin [24], some active marks can persist through mitosis and support post-mitotic reactivation [66]. Our model provides a general framework for predicting whether a marked state can recover from these perturbations. Strict memory behavior occurs only in the MEMORY regime, where mark dilution can be repaired provided that the perturbed state remains above m_{U} and within the high-mark basin. This basin expands as a increases, allowing progressively greater mark loss to be tolerated, whereas falling below m_{U} results in loss of the marked state.

More generally, regulatory inputs in living cells vary in amplitude and duration in response to environmental stimuli, developmental programs, and intracellular signals [55–57]. Under these conditions, the response of active chromatin also depends on the competition between the timescales of regulatory input and mark dynamics. Even under a simple periodic input, our model generates frequency-dependent hysteresis, and the measured $\mathcal{G}$ also quantitatively predicts the simulated loops without additional fitting. Across stimulus amplitudes and frequencies, the response separates into nonresponsive, direct-response, and temporal-integration regimes. In the temporal-integration regime, individual stimulation cycles are insufficient for establishment, but residual marks accumulate over repeated cycles until activation occurs. These behaviors provide a possible physical framework for chromatin-based transcriptional memory under repeated stimulation [33–35, 67].

The present model only considers a single generic epigenetic state, a single chromatin segment, and a coarse-grained description of writing-related trans-

factors. These limitations also indicate natural directions for extension. Multiple chromatin regions coupled through three-dimensional contacts and a shared factor pool could exhibit competitive or cooperative behavior, allowing regulatory signals to be encoded in a network of spatially interacting chromatin states. Such an extension could provide an epigenetic-state framework for enhancer–promoter communication [68, 69]. The same separation between external input and state-dependent spatial feedback may also be applied to HP1- or Polycomb-mediated repressive systems, complementing existing models of state inheritance with an explicit treatment of changing regulatory conditions [19, 20]. In these systems, the central question shifts toward how epigenetic states are transmitted and remodeled across cell divisions [7, 16, 17, 70]. Addressing this problem will require extending the framework to multiple chromatin regions coupled through three-dimensional contact networks that, unlike transient enhancer–promoter contacts, can form more persistent and stable spatial organizations. More broadly, our results suggest a design principle for nonequilibrium signal processing: coupling an external drive to a positive feedback loop enables a stochastic system to discriminate signal strength, retain history, and integrate time-dependent inputs.

ACKNOWLEDGMENTS

We thank Profs. Zhong-Yuan Lu (Jilin University) for helpful discussion. We acknowledge computational support from the Shenzhen Bay Laboratory High Performance Computing and Informatics Core. This work was funded by grants from the National Natural Science Foundation of China (nos. 32521002 and 32571445), and the Shenzhen Medical Research Fund (B2602069).

[1] R. Bonasio, S. Tu, and D. Reinberg, Molecular signals of epigenetic states, Science **330**, 612 (2010).
[2] C. D. Allis and T. Jenuwein, The molecular hallmarks of epigenetic control, Nat. Rev. Genet. **17**, 487 (2016).
[3] G. Cavalli and E. Heard, Advances in epigenetics link genetics to the environment and disease, Nature **571**, 489 (2019).
[4] A. V. Probst, E. Dunleavy, and G. Almouzni, Epigenetic inheritance during the cell cycle, Nat. Rev. Mol. Cell Biol. **10**, 192 (2009).
[5] R. Cortini, M. Barbi, B. R. Caré, C. Lavelle, A. Lesne, J. Mozziconacci, and J.-M. Victor, The physics of epigenetics, Rev. Mod. Phys. **88**, 025002 (2016).
[6] D. Michieletto, D. Colì, D. Marenduzzo, and E. Orlandini, Nonequilibrium theory of epigenomic microphase separation in the cell nucleus, Phys. Rev. Lett. **123**, 228101 (2019).
[7] J. A. Owen, D. Osmanović, and L. Mirny, Design principles of 3D epigenetic memory systems, Science **382**, eadg3053 (2023).
[8] J. A. Owen and L. A. Mirny, Chromatin as a three-dimensional memory machine, Curr. Opin. Struct. Biol. **95**, 103160 (2025).
[9] G. Forte, C. A. Brackley, N. Gilbert, and D. Marenduzzo, Nonequilibrium polymer models for chromatin, Curr. Opin. Genet. Dev. **96**, 102426 (2026).
[10] G. Spracklin, N. Abdennur, M. Imakaev, N. Chowdhury, S. Pradhan, L. A. Mirny, and J. Dekker, Diverse silent chromatin states modulate genome compartmentalization and loop extrusion barriers, Nat. Struct. Mol. Biol. **30**, 38 (2023).
[11] I. B. Dodd, M. A. Micheelsen, K. Sneppen, and G. Thon, Theoretical analysis of epigenetic cell memory by nucleosome modification, Cell **129**, 813 (2007).
[12] R. Margueron, N. Justin, K. Ohno, M. L. Sharpe, J. Son, W. J. Drury Iii, P. Voigt, S. R. Martin, W. R. Taylor, V. De Marco, V. Pirrotta, D. Reinberg, and S. J. Gamblin, Role of the polycomb protein EED in the propagation of repressive histone marks, Nature **461**, 762 (2009).
[13] M. M. Müller, B. Fierz, L. Bittova, G. Liszczak, and T. W. Muir, A two-state activation mechanism controls the histone methyltransferase Suv39h1, Nat. Chem. Biol. **12**, 188 (2016).
[14] M. Ciapponi, E. Karlukova, S. Schkölziger, C. Benda, and J. Müller, Structural basis of the histone ubiquitination read–write mechanism of RYBP–PRC1, Nat. Struct. Mol. Biol. **31**, 1023 (2024).
[15] J. Dekker and L. A. Mirny, The chromosome folding problem and how cells solve it, Cell **187**, 6424 (2024).
[16] D. Michieletto, E. Orlandini, and D. Marenduzzo, Polymer model with epigenetic recoloring reveals a pathway for the de novo establishment and 3D organization of chromatin domains, Phys. Rev. X **6**, 041047 (2016).
[17] D. Michieletto, M. Chiang, D. Colì, A. Papantonis, E. Orlandini, P. R. Cook, and D. Marenduzzo, Shaping epigenetic memory via genomic bookmarking, Nucleic Acids Res. **46**, 83 (2018).
[18] S. H. Sandholtz, Q. MacPherson, and A. J. Spakowitz, Physical modeling of the heritability and maintenance of epigenetic modifications, Proc. Natl. Acad. Sci. **117**, 20423 (2020).
[19] S. Mukherjee, E. Skoruppa, H. Merlitz, J.-U. Sommer, and H. Schiessel, A self-organized liquid reaction container for cellular memory, Adv. Sci. **13**, e12500 (2026).
[20] A. Berard, J. R. Gissinger, K. Sneppen, and G. Thon, Epigenetic memory achieved through chromatin-induced phase separation, PRX Life **4**, 033016 (2026).
[21] A. J. Bannister and T. Kouzarides, Regulation of chromatin by histone modifications, Cell Res. **21**, 381 (2011).
[22] T. K. Barth and A. Imhof, Fast signals and slow marks: the dynamics of histone modifications, Trends Biochem. Sci. **35**, 618 (2010).
[23] Y. Zheng, P. M. Thomas, and N. L. Kelleher, Measurement of acetylation turnover at distinct lysines in human histones identifies long-lived acetylation sites, Nat. Commun. **4**, 2203 (2013).
[24] T. M. Escobar, O. Oksuz, R. Saldaña-Meyer, N. Descostes, R. Bonasio, and D. Reinberg, Active and Re-

pressed Chromatin Domains Exhibit Distinct Nucleosome Segregation during DNA Replication, Cell **179**, 953 (2019).

[25] S. Henikoff and A. Shilatifard, Histone modification: cause or cog?, Trends Genet. **27**, 389 (2011).

[26] B. J. E. Martin, J. Brind'Amour, A. Kuzmin, K. N. Jensen, Z. C. Liu, M. Lorincz, and L. J. Howe, Transcription shapes genome-wide histone acetylation patterns, Nat. Commun. **12**, 210 (2021).

[27] Z. Wang, A. G. Chivu, L. A. Choate, E. J. Rice, D. C. Miller, T. Chu, S.-P. Chou, N. B. Kingsley, J. L. Petersen, C. J. Finno, R. R. Bellone, D. F. Antczak, J. T. Lis, and C. G. Danko, Prediction of histone post-translational modification patterns based on nascent transcription data, Nat. Genet. **54**, 295 (2022).

[28] L.-F. Chen, Y. T. Lin, D. A. Gallegos, M. F. Hazlett, M. Gómez-Schiavon, M. G. Yang, B. Kalmeta, A. S. Zhou, L. Holtzman, C. A. Gersbach, J. Grandl, N. E. Buchler, and A. E. West, Enhancer Histone Acetylation Modulates Transcriptional Bursting Dynamics of Neuronal Activity-Inducible Genes, Cell Rep. **26**, 1174 (2019).

[29] L. Patel, Y. Cao, T. Xu, E. Modolo, T. Dishon, L. Zhang, E. Mendenhall, S. Heinz, I. Simon, C. Benner, and A. Goren, Improved spike-in normalization clarifies the relationship between active histone modifications and transcription, bioRxiv 10.1101/2025.11.25.690627 (2026).

[30] J. A. Hoffman, K. W. Trotter, and T. K. Archer, RNA polymerase II coordinates histone deacetylation at active promoters, Sci. Adv. **11**, eadt3037 (2025).

[31] T. Liebner, S. Kilic, J. Walter, H. Aibara, T. Narita, and C. Choudhary, Acetylation of histones and non-histone proteins is not a mere consequence of ongoing transcription, Nat. Commun. **15**, 4962 (2024).

[32] K. C. Palozola, J. Lerner, and K. S. Zaret, A changing paradigm of transcriptional memory propagation through mitosis, Nat. Rev. Mol. Cell Biol. **20**, 55 (2019).

[33] Y. He and Z. Li, Epigenetic environmental memories in plants: establishment, maintenance, and reprogramming, Trends Genet. **34**, 856 (2018).

[34] P. Mikulski, S. S. H. Tehrani, A. Kogan, I. Abdul-Zani, E. Shell, L. James, B. J. Ryan, and L. E. T. Jansen, Heritable maintenance of chromatin modifications confers transcriptional memory of interferon-γ signaling, Nat. Struct. Mol. Biol. **32**, 1255 (2025).

[35] S. S. H. Tehrani, A. Kogan, P. Mikulski, and L. E. T. Jansen, Remembering foods and foes: emerging principles of transcriptional memory, Cell Death Differ. **32**, 16 (2025).

[36] Z. Ibrahim, T. Wang, O. Destaing, N. Salvi, N. Hoghoughi, C. Chabert, A. Rusu, J. Gao, L. Feletto, N. Reynoird, *et al.*, Structural insights into p300 regulation and acetylation-dependent genome organisation, Nat. Commun. **13**, 7759 (2022).

[37] M. Kikuchi, S. Morita, M. Wakamori, S. Sato, T. Uchikubo-Kamo, T. Suzuki, N. Dohmae, M. Shirouzu, and T. Umehara, Epigenetic mechanisms to propagate histone acetylation by p300/CBP, Nat. Commun. **14**, 4103 (2023).

[38] B. R. Sabari, A. Dall'Agnese, A. Boija, I. A. Klein, E. L. Coffey, K. Shrinivas, B. J. Abraham, N. M. Hannett, A. V. Zamudio, J. C. Manteiga, C. H. Li, Y. E. Guo, D. S. Day, J. Schuijers, E. Vasile, S. Malik, D. Hnisz, T. I. Lee, I. I. Cisse, R. G. Roeder, P. A. Sharp, A. K. Chakraborty, and R. A. Young, Coactivator condensation at super-enhancers links phase separation and gene control, Science **361**, eaar3958 (2018).

[39] M. N. Saxton, T. Morisaki, D. Krapf, H. Kimura, and T. J. Stasevich, Live-cell imaging uncovers the relationship between histone acetylation, transcription initiation, and nucleosome mobility, Sci. Adv. **9**, eadh4819 (2023).

[40] Y. Zhang, K. Brown, Y. Yu, Z. Ibrahim, M. Zandian, H. Xuan, S. Ingersoll, T. Lee, C. C. Ebmeier, J. Liu, D. Panne, X. Shi, X. Ren, and T. G. Kutateladze, Nuclear condensates of p300 formed though the structured catalytic core can act as a storage pool of p300 with reduced HAT activity, Nat. Commun. **12**, 4618 (2021).

[41] M. Kosno, S. L. Currie, A. Kumar, C. Xing, and M. K. Rosen, Molecular features driving condensate formation and gene expression by the BRD4-NUT fusion oncoprotein are overlapping but distinct, Sci. Rep. **13**, 11907 (2023).

[42] A. R. Strom, J. M. Eeftens, Y. Polyachenko, C. J. Weaver, H.-F. Watanabe, D. Bracha, N. D. Orlovsky, C. C. Jumper, W. M. Jacobs, and C. P. Brangwynne, Interplay of condensation and chromatin binding underlies BRD4 targeting, Mol. Biol. Cell **35**, ar88 (2024).

[43] Y. Polyachenko, H.-F. Watanabe, A. Korolev, and W. M. Jacobs, Co-condensation and multivalency enable acetylation-sensitive, concentration-robust assembly of BRD4 condensates (2026), arXiv:2606.02275 [physics.bio-ph].

[44] T. Narita, S. Ito, Y. Higashijima, W. K. Chu, K. Neumann, J. Walter, S. Satpathy, T. Liebner, W. B. Hamilton, E. Maskey, G. Prus, M. Shibata, V. Iesmantavicius, J. M. Brickman, K. Anastassiadis, H. Koseki, and C. Choudhary, Enhancers are activated by p300/CBP activity-dependent PIC assembly, RNAPII recruitment, and pause release, Mol. Cell **81**, 2166 (2021).

[45] B. M. Zee, R. S. Levin, P. A. DiMaggio, and B. A. Garcia, Global turnover of histone post-translational modifications and variants in human cells, Epigenet. Chromatin **3**, 22 (2010).

[46] A. S. Novozhilov, G. P. Karev, and E. V. Koonin, Biological applications of the theory of birth-and-death processes, Briefings Bioinf. **7**, 70 (2006).

[47] S. Bruno and D. Del Vecchio, Stochastic modeling of epigenetic memory, npj Syst. Biol. Appl. **12**, 58 (2026).

[48] S. Heinz, C. E. Romanoski, C. Benner, and C. K. Glass, The selection and function of cell type-specific enhancers, Nat. Rev. Mol. Cell Biol. **16**, 144 (2015).

[49] J. A. Anderson, J. Glaser, and S. C. Glotzer, HOOMD-blue: A Python package for high-performance molecular dynamics and hard particle Monte Carlo simulations, Comput. Mater. Sci. **173**, 109363 (2020).

[50] See Supplemental Material for details of the microscopic model and simulation methods, measurement and validation of the conditional enrichment, derivations of the finite-system birth–death dynamics, and procedures for perturbation, activation–maintenance, and periodic stimulation.

[51] S. Karlin, *A first course in stochastic processes* (Academic press, 2014).

[52] M. A. Micheelsen, N. Mitarai, K. Sneppen, and I. B. Dodd, Theory for the stability and regulation of epigenetic landscapes, Phys. Biol. **7**, 026010 (2010).

[53] T. Formosa and F. Winston, The role of FACT in manag-

ing chromatin: disruption, assembly, or repair?, Nucleic Acids Res. **48**, 11929 (2020).

[54] K. R. Stewart-Morgan, N. Petryk, and A. Groth, Chromatin replication and epigenetic cell memory, Nat. Cell Biol. **22**, 361 (2020).

[55] K. Wagh, D. A. Stavreva, A. Upadhyaya, and G. L. Hager, Transcription factor dynamics: one molecule at a time, Annu. Rev. Cell Dev. Biol. **39**, 277 (2023).

[56] M. A. Gillespie, C. G. Palii, D. Sanchez-Taltavull, P. Shannon, W. J. Longabaugh, D. J. Downes, K. Sivaraman, H. M. Espinoza, J. R. Hughes, N. D. Price, *et al.*, Absolute quantification of transcription factors reveals principles of gene regulation in erythropoiesis, Mol. Cell **78**, 960 (2020).

[57] P. Yang, C. Mathieu, R.-M. Kolaitis, P. Zhang, J. Messing, U. Yurtsever, Z. Yang, J. Wu, Y. Li, Q. Pan, *et al.*, G3BP1 is a tunable switch that triggers phase separation to assemble stress granules, Cell **181**, 325 (2020).

[58] M. Du, S. H. Stitzinger, J.-H. Spille, W.-K. Cho, C. Lee, M. Hijaz, A. Quintana, and I. I. Cissé, Direct observation of a condensate effect on super-enhancer controlled gene bursting, Cell **187**, 331 (2024).

[59] Z. Wu, S. D. Pope, N. S. Ahmed, D. L. Leung, Y. Hong, S. Hajjar, C. Krabak, Z. Zhong, K. Raghunathan, Q. Yue, *et al.*, Regulation of inflammatory responses by pH-dependent transcriptional condensates, Cell **188**, 5632 (2025).

[60] N. U. Erdogdu, S. Guhathakurta, R. Oellers, M. Shvedunova, J. A. Morin, E. M. Patrick, J. Seyfferth, W. Deboutte, A. Gomez-Auli, G. Mittler, *et al.*, Histone acetylation-dependent clustering of BRD2 instructs transcription dynamics, Nat. Genet. **58**, 854 (2026).

[61] A. Boija, I. A. Klein, B. R. Sabari, A. Dall'Agnese, E. L. Coffey, A. V. Zamudio, C. H. Li, K. Shrinivas, J. C. Manteiga, N. M. Hannett, *et al.*, Transcription factors activate genes through the phase-separation capacity of their activation domains, Cell **175**, 1842 (2018).

[62] D. Hay, J. R. Hughes, C. Babbs, J. O. Davies, B. J. Graham, L. L. Hanssen, M. T. Kassouf, A. M. Oudelaar, J. A. Sharpe, M. C. Suciu, *et al.*, Genetic dissection of the α-globin super-enhancer in vivo, Nat. Genet. **48**, 895 (2016).

[63] M. Osterwalder, I. Barozzi, V. Tissières, Y. Fukuda-Yuzawa, B. J. Mannion, S. Y. Afzal, E. A. Lee, Y. Zhu, I. Plajzer-Frick, C. S. Pickle, *et al.*, Enhancer redundancy provides phenotypic robustness in mammalian development, Nature **554**, 239 (2018).

[64] R. P. DeKoter and H. Singh, Regulation of B lymphocyte and macrophage development by graded expression of PU. 1, Science **288**, 1439 (2000).

[65] S. Wang, J. Yan, D. A. Anderson, Y. Xu, M. C. Kanal, Z. Cao, C. V. Wright, and G. Gu, Neurog3 gene dosage regulates allocation of endocrine and exocrine cell fates in the developing mouse pancreas, Dev. Biol. **339**, 26 (2010).

[66] B. Pelham-Webb, A. Polyzos, L. Wojenski, A. Kloetgen, J. Li, D. C. Di Giammartino, T. Sakellaropoulos, A. Tsirigos, L. Core, and E. Apostolou, H3K27ac bookmarking promotes rapid post-mitotic activation of the pluripotent stem cell program without impacting 3D chromatin reorganization, Mol. Cell **81**, 1732 (2021).

[67] R. Ostuni, V. Piccolo, I. Barozzi, S. Polletti, A. Termanini, S. Bonifacio, A. Curina, E. Prosperini, S. Ghisletti, and G. Natoli, Latent enhancers activated by stimulation in differentiated cells, Cell **152**, 157 (2013).

[68] J. Zuin, G. Roth, Y. Zhan, J. Cramard, J. Redolfi, E. Piskadlo, P. Mach, M. Kryzhanovska, G. Tihanyi, H. Kohler, *et al.*, Nonlinear control of transcription through enhancer–promoter interactions, Nature **604**, 571 (2022).

[69] X. Lin, Y. Liu, S. Liu, X. Zhu, L. Wu, Y. Zhu, D. Zhao, X. Xu, A. Chemparathy, H. Wang, *et al.*, Nested epistasis enhancer networks for robust genome regulation, Science **377**, 1077 (2022).

[70] A. Movilla Miangolarra, D. S. Saxton, Z. Yan, J. Rine, and M. Howard, Two-way feedback between chromatin compaction and histone modification state explains saccharomyces cerevisiae heterochromatin bistability, Proc. Natl. Acad. Sci. **121**, e2403316121 (2024).

[71] A. Valouev, S. M. Johnson, S. D. Boyd, C. L. Smith, A. Z. Fire, and A. Sidow, Determinants of nucleosome organization in primary human cells, Nature **474**, 516 (2011).

[72] S. C. Parker, M. L. Stitzel, D. L. Taylor, J. M. Orozco, M. R. Erdos, J. A. Akiyama, K. L. Van Bueren, P. S. Chines, N. Narisu, N. C. S. Program, *et al.*, Chromatin stretch enhancer states drive cell-specific gene regulation and harbor human disease risk variants, Proc. Natl. Acad. Sci. **110**, 17921 (2013).

[73] W. A. Whyte, D. A. Orlando, D. Hnisz, B. J. Abraham, C. Y. Lin, M. H. Kagey, P. B. Rahl, T. I. Lee, and R. A. Young, Master transcription factors and mediator establish super-enhancers at key cell identity genes, Cell **153**, 307 (2013).

[74] S. Kadam, K. Kumari, V. Manivannan, S. Dutta, M. K. Mitra, and R. Padinhateeri, Predicting scale-dependent chromatin polymer properties from systematic coarse-graining, Nat. Commun. **14**, 4108 (2023).

[75] A. M. Chiariello, A. Abraham, S. Bianco, A. Esposito, A. Fontana, F. Vercellone, M. Conte, and M. Nicodemi, Multiscale modelling of chromatin 4D organization in SARS-CoV-2 infected cells, Nat. Commun. **15**, 4014 (2024).

[76] D. T. Gillespie, Exact stochastic simulation of coupled chemical reactions, J. Phys. Chem. **81**, 2340 (1977).